2 PF Ring

2-1 Summary of Machine Operations

The operation statistics of the PF ring for FY2004 are tabulated in Table 1, and Fig.1 shows the ring operation time, scheduled user time and actual user time since 1982. The total operation time for FY2004 of 4864 hours was appreciably shorter than for FY2003 because the ring was closed one month before the end of FY2004 in order to start the straight-sections upgrade project, described in the next section. In FY2004, the scheduled user time was 4080 hours, and the actual user time excluding time losses due to machine trouble and daily injections was 3999 hours. The ratio of actual user time to scheduled time has been maintained at 96-98% over the past 5 years. Fig. 2 shows the trend of the product $I\tau$ of the beam current I and the beam lifetime τ over the past 8 years, and Fig. 3 shows the history of the average stored beam current since 1982. Although the initial beam current has not been changed for several years, a gradual increase in the average beam current corresponding to an increase in the $I\tau$ product is noticeable.

The change in the failure rate, defined as the ratio of failure time to the total operation time, is shown in Fig. 4. The failure rate has been maintained at around 1% over the past 10 years, and about 0.5% over the past 3 years. This high reliability has been realized by the ceaseless efforts of the staff of the light source division and the operators to keep the machine in good condition. However, old components are still in use in several areas. Some of these will be renewed as part of the straight-sections upgrade project.

For the usual multibunch operation at 2.5 GeV, the lifetime was long enough to allow for once per day (9 a.m.) injection. The initial beam current of 450 mA in this mode was unchanged throughout the year, however, in 3 GeV mode the beam current was restricted to 200 mA, due to the limited RF power available. On the other hand, during single-bunch mode operations the ring was injected three times a day because the Touschek effect limits the beam lifetime and the beam current drops from an initial current of 70 mA to about 30 mA 8 hours after injection.
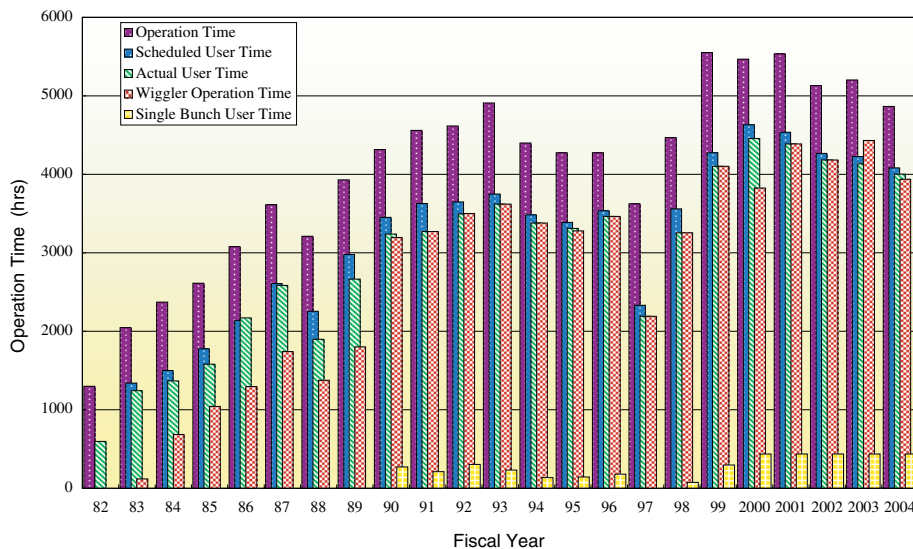

Figure 1
Operation time history of the PF Storage Ring.

Table 1 Statistics of the PF Storage Ring operation during FY2004.

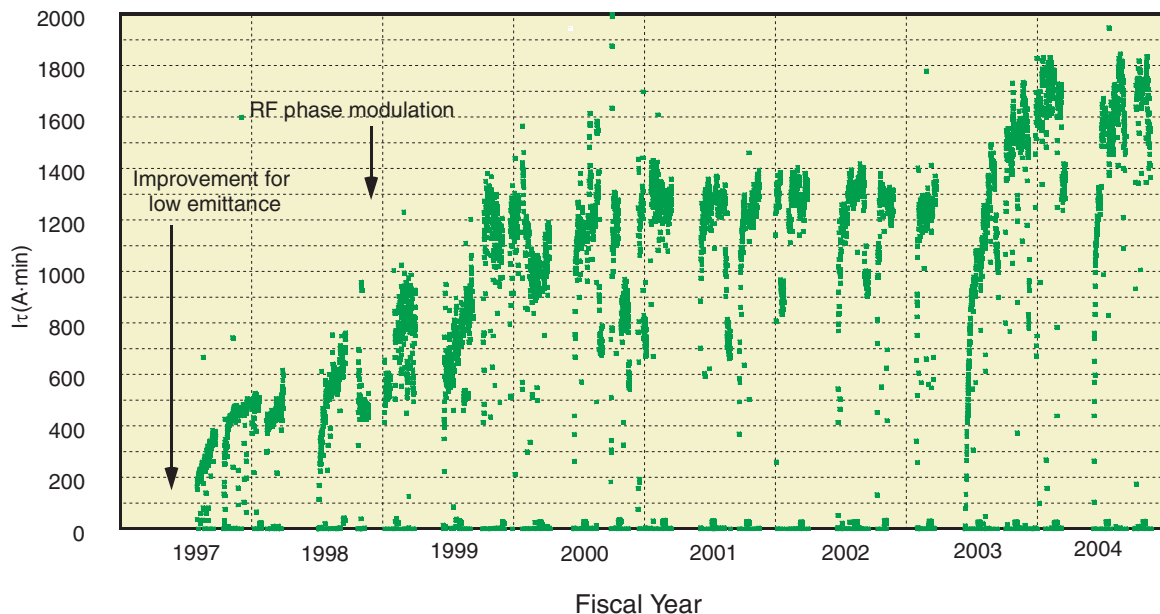|	Multi-bunch	Single-bunch	Total
Ring Operation Time (hours)	4432.0	432.0	4864.0
Scheduled user time (hours)	3648.0	432.0	4080.0
Actual user time T (hours)	3585.6	413.7	3999.3
Time used for injection (hours)	41.0	14.6	55.6
Integrated current in T (A·hours)	1294.9	18.8	1313.7
Average current in T (mA)	361.1	45.4	--
Number of injections	168	58	226
Average interval between injections (hours)	21.3	7.1	--

Figure 2
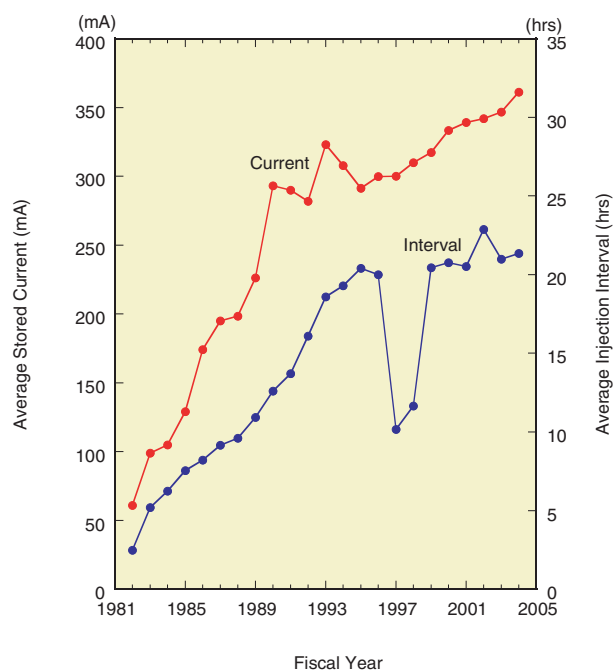Iτ history of the PF Storage Ring over the past 7 years.

Figure 3
Average stored current and injection interval since 1982.
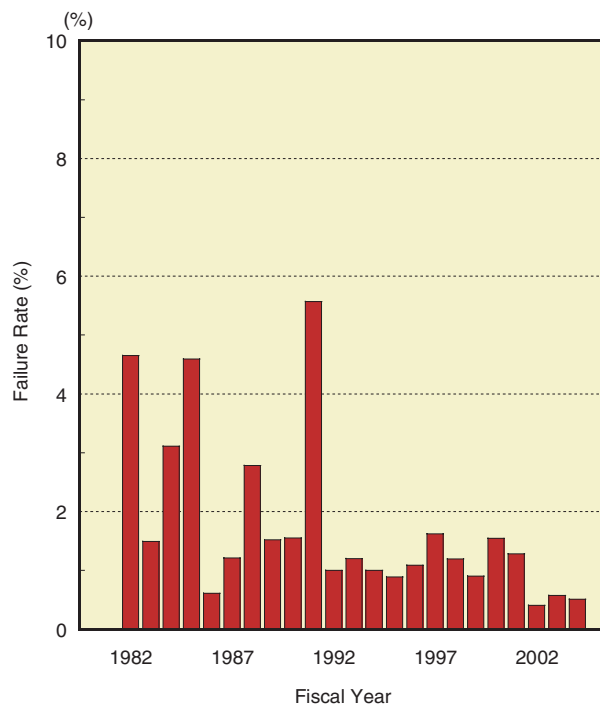

Figure 4
Failure rate history.

2-2 Straight-Sections Upgrade Project

Progress of the reconstruction work of the storage ring

The straight-sections upgrade project of the 2.5 GeV ring has been under way since 2002, beginning with a remodeling of three beamline front-ends. As described in previous reports [1], the purposes of the project are the creation of four new straight sections and the extension of the existing straight sections. The areas of the storage ring to be reconstructed are illustrated in Fig. 5. In the existing straight sections, all quadrupole magnets will be replaced by new ones of shorter length and higher field gradient. Forty six new quadrupoles have been manufactured for the project. The beam ducts for the quadrupoles and for the twelve bending magnets will be also replaced by newly designed ones. The additional straight sections will be utilized for short gap undulators suitable for X-ray research fields. Renewal of the existing insertion devices will also be promoted for the extended straight sections. The manufacturing of the new quadrupole magnets was carried out in FY2003, and the design and manufacturing of the beam ducts was completed in FY2004. The remodeling of the beamline front-ends has continued during every scheduled shutdown period. Basic parameters of the beamline front-ends after the reconstruction are
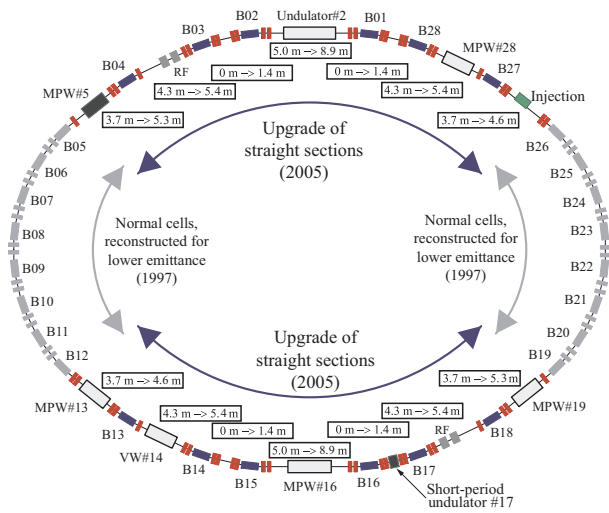
Figure 5
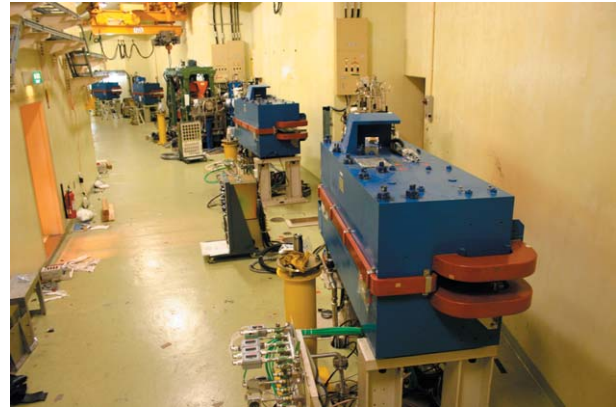Straight-sections area to be reconstructed for the upgrade project.

Figure 6
The old quadrupoles and beam ducts were completely removed from the straight-section area. The bending magnets and the existing insertion devices were left behind in the ring tunnel.

summarized in Table 2.

The reconstruction work of the storage ring started in March 2005, and the shutdown for the reconstruction is planned to last about 7 months. Commissioning will begin in the middle of September 2005, and user operation will resume after four weeks of machine adjustment and vacuum scrubbing.

During the first stage of the reconstruction, all quadrupole magnets and beam ducts were removed from the straight sections. Only the bending magnets and the existing insertion devices were left behind, as shown in Fig. 6. The new quadrupole magnets were then installed at modified positions close to the nearby bending mag-

Table 2 Basic parameters of the beamline front ends. (After the completion of the upgrade.)
Reference name of the beamline, type of the light source, horizontal and vertical opening angles and its angular sharing by branch beamlines are summarized.
[0] BL: Beamline, LS: Type of the light source.
[1] Source point of the insertion device is assumed to be at the center of the device along the beam axis.
[2] Source point of the vertical wiggler is assumed to be at 1200–5.4 mm in height. Others at 1200 mm.
[3] Opening angles shared by the branches are measured A: from the downstream edge of B02 bending magnet and B,C: from the upstream edge of B03 bending magnet. The vertical opening angle is measured from the latter point.

BL	LS	Central Axis (deg)	Full Opening Angle Horizontal (mrad)	Full Opening Angle Vertical (mrad)	Beam sharing by branch beamlines				[0]
					A(mrad)	B(mrad)	C(mrad)	D(mrad)	
BL-1	B	2.5	−18 : +18	−1.75 : +1.75	−17 : −14	+6 : +9	+11 : +16		
BL-2	U	0	−0.875 : +0.875	−0.8 : +0.8	−0.1 : +0.1		−0.1 : +0.1		[1]
BL-3	B	0	−8.5 : +18.5	−1.75 : +1.75	−8.5 : −4.5	+3.5 : +13.5	+16.5 : +18.5		[3]
BL-4	B	2.5	−18 : +18	−1.75 : +1.75	−16 : −12	−1.5 : +1.5	+12.5 : +15.5		
BL-5	MPW	0	−1.7 : +1.7	−1.2 : +1.2					[1]
BL-6	B	2.5	−17 : +17	−1.61 : +1.61	−16.5 : −12.5	0 : +4	+12.5 : +16.5		
BL-7	B	2.5	−18 : +18	−2 : +2	−16.5 : −10.5	+5 : +11	+13 : +17		
BL-8	B	2.5	−17 : +17	−2 : +2	−16 : −15	−6.5 : −3.5	+11 : +16	+6 : +8	
BL-9	B	2.5	−18 : +9.5	−2 : +2	−16.9 : −11.9	−8.8 : +1.2	+3.1 : +9.1		
BL-10	B	2.5	−13.5 : +13.5	−1.5 : +1.5	−13 : −8.5	−1.75 : +0.25	+7 : +13		
BL-11	B	2.5	−13.5 : +13.5	−1.27 : +1.27	−15 : −10	−7 : −3	−1 : +4	+7 : +11	
BL-12	B	2.5	−12 : +12	−1.5 : +1.5	−11 : −8	−3 : +2	+6 : +11		
BL-13	MPW	0	−3 : +3	−1 : +1					[1]
BL-14	VW	0	−0.5815 : +0.5815	−2.27 : +5.07	−2.27 : −0.96	+0.84 : +1.70	+3.12 : +5.07		[2]
BL-15	B	2.5	−13.75 : +13.75	−1.5 : +1.5	−13 : −8.5	−1.75 : +0.25	+7 : +13		
BL-16	MPW/U	0	−1.8 : +1.8	−0.6 : +0.6	−0.5 : +0.5	−0.9 : +0.9			[1]
BL-17	SGU	0	−2.4 : +2.4	−1.4 : +1.4					[1]
BL-18	B	2.5	−13.2 : +13.2	−1.75 : +1.75	−13 : −7.2	−2.9 : +2.9	+7.2 : +13		
BL-19	U	0	−2.13 : +2.13	−0.75 : +0.75	−0.6 : +0.6				[1]
BL-20	B	2.5	−19 : +16	−2 : +2	−19 : +9	+14 : +16			
BL-27	B	1.2	−8.5 : +8.5	−0.9 : +0.9	−8 : −3	+4 : +8			
BL-28	MPW/U	0	−2.2 : +2.2	−1 : +1					[1]

Figure 7
Images before (top) and after (bottom) the rearrangement of the quadrupoles where the short straight section is created.

Figure 8
Images before (top) and after (bottom) the rearrangement of the quadrupoles around MPW#16. Free spaces of 2 m long are created at either end of MPW#16.

nets. Fig. 7 shows the section between bending magnets #28 and #01, where a new short straight section has been created. The upper image of Fig. 7 shows the previous arrangement, and the lower image shows the new quadrupole arrangement, just before installation of beam ducts. Fig. 8 shows the rearrangement of the quadrupoles around MPW#16. Free spaces of about 2 m long have been created at either end of MPW#16.

Following the installation of the new quadrupoles, installation of the new beam ducts continues. The first new short gap undulator will be installed for beamline #17. The power supplies for the quadrupoles will be reinforced, and the number of corrector magnets and beam position monitors will be increased. Along with reinforcement of the hardware, improvements of the control systems for the magnets, RF and vacuum systems are in progress, using the EPICS environment.

References
[1] *Photon Factory Activity Report 2002*, **19A** (2001) 82.
     Photon Factory Activity Report 2003, **20A** (2002) 97.

### Installation and alignment of the quadrupole magnets

We measured the coordinates of all the magnets in the PF ring during the summer shutdown of 2004. We used a leveling scope for the vertical survey and a laser tracker for the horizontal survey. The laser tracker was used for the first time for the alignment of the PF ring. The purpose of the measurement was to establish the survey procedure, and to align the quadrupole magnets for the straight sections upgrade project in 2005. We also aimed to obtain standard coordinates for the present magnetic lattice in order to calculate the ring geometry.

A photograph showing the survey work taking place is given in Fig. 9. We divided the ring into fifteen survey partitions, and local coordinates were determined for all of the magnets within each partition. In each local survey, about ten points from the neighboring partitions were re-measured to provide tie-point references for later

Figure 9
Coordinate survey using the laser tracker system.

(a) Results of the local measurement
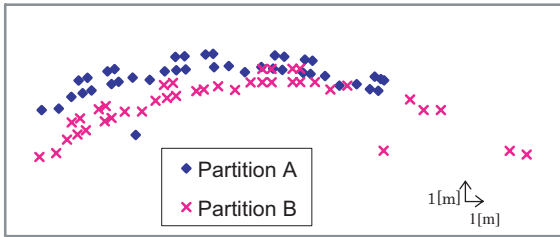
(b) After the coordinate transformation
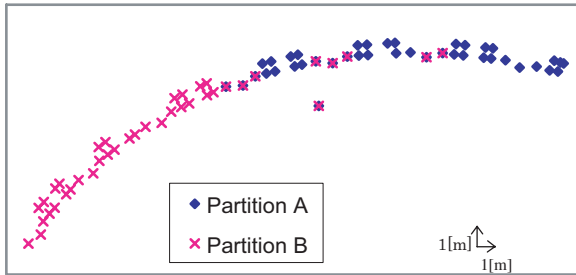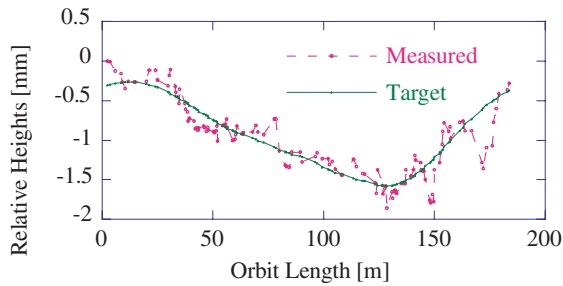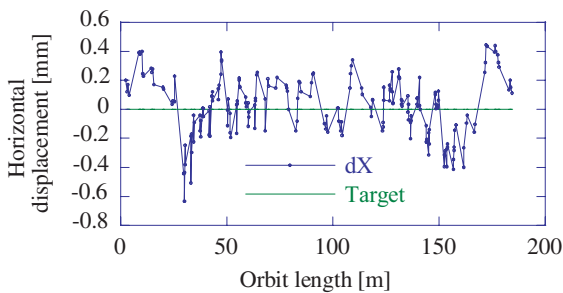

Figure 10
Results of the coordinate transformation.

(a) Vertical heights of the magnets

(b) Horizontal displacement (ring outside positive)

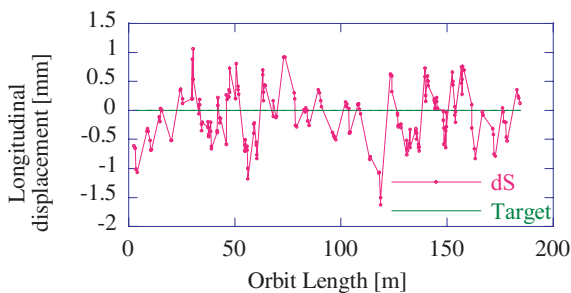(c) Longitudinal position (upstream positive)

Figure 11
Analyzed results of the survey.

analysis. Finally the measured results from all of the local surveys were integrated by the use of a coordinate transformation overlapping the tie-points, as shown in Fig. 10.

Figure 12
The old quadrupole magnets.

Figure 13
The base plate of the magnet girder.

The analyzed results of the vertical survey are shown in Fig. 11(a), and those from the horizontal survey in figures 11(b) and (c). The measurement errors of the coordinate surveys were estimated to be about 30 μm from the results of the analysis.

For the straight-sections upgrade project, the target coordinates for the new quadrupole magnets will be calculated based on the survey results. The coordinates of each bending magnet and the monument (the pillar with the survey target standing in front of each bending magnet) are used as reference points for the magnet alignment. The new magnets will be aligned vertically so that the vertical orbit of the electron is on an identical plane and agrees with the previous orbit as well as possible. On the other hand, the horizontal coordinates will be fixed to the ideal orbit without any distortion.

Forty-six new quadrupole magnets have been manufactured and twenty-one magnet girders prepared. Thirty-six of the magnets are doublets, with two quadrupole magnets on the same girder. For the doublets, the relative positions, directions and levels of the two magnets will be precisely aligned on the girder before installation into the ring tunnel, after which the alignment of the quadrupole magnets will be achieved by adjusting the

Figure 14
Installation of a new quadrupole magnet.

girder positions.

We removed all of the old quadrupole magnets from the straight sections in March 2005 (Fig. 12). After the base plates for the new magnet girders were firmly laid on the tunnel floor (Fig. 13), the new quadrupole magnets, mounted on the new girders were installed into the ring tunnel (Fig. 14). The manufacturing accuracy of the quadrupole magnet core is about 20 μm, and the alignment of the quadrupole magnets has been accomplished with an error smaller than the maximum tolerable value of 100 μm.

New power supplies for the quadrupole magnets

As part of the straight-section upgrade project the configuration of the power supplies for the quadrupole magnets has been changed. Previously, fifteen power supplies were employed for the quadrupole magnets. The number of optical families for the quadrupole magnets was twenty-three, but that of the power supplies was fifteen. In the upgrade, eight of the old power supplies were removed and sixteen new power supplies were introduced. Thus, we have twenty-three power supplies at present.

The previous configuration of the quadrupole magnets is shown in Fig. 15. Several quadrupole magnets of different families were connected to the same power supply in some cases, as shown in Table 3. In these cases,
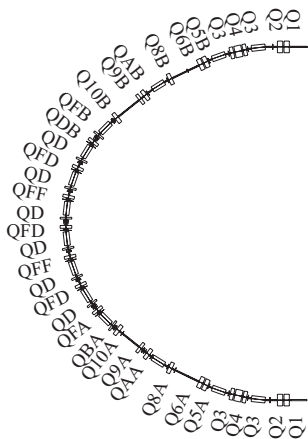
Table 3
List of the power supplies before the upgrade.

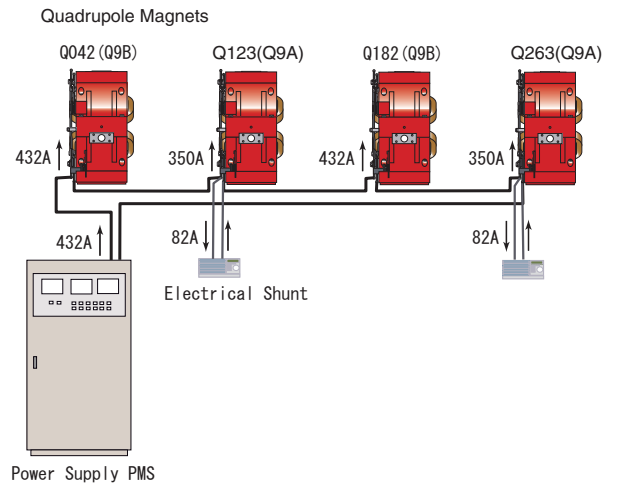| Q-mag family name	Power supply name	Type	Date of manu-facture	Maximum current [A]	Maximum voltage [V]	Capacity [kW]
Q1	P2S	SCR	1986	440	90	39.6
Q2	P3S	SCR	1986	520	150	78
Q3	PAS	SCR	1990	610	180	109.8
Q4	PCS	SCR	1990	760	180	136.8
Q5A Q5B	PBS shunt	SCR	1990	470	100	39.6
Q6A Q6B	P4S shunt	SCR	1986	610	150	39.6
Q8A Q8B	P6S shunt	SCR	1986	450	80	39.6
QAA QAB	PNS shunt	SCR	1997	600	130	39.6
Q9A Q9B	PMS shunt	SCR	1997	700	80	39.6
Q10A	PIS	SCR	1997	450	50	22.5
Q10B	PJS	SCR	1997	450	50	22.5
QFD	PHS	SCR	1997	900	190	171
QFF QFA QFB	PDS shunt shunt	SCR	1997	900	150	39.6
QBA	PES	SCR	1997	900	45	40.5
QD QDB	PFS shunt	SCR	1997	900	250	39.6
SFF	PKS	SCR	1997	450	140	63
SFD	PLS	SCR	1997	450	140	63
SD	PGS	SCR	1997	450	260	117

Figure 16
The power supply system with electrical shunts (before upgrade).

Figure 15
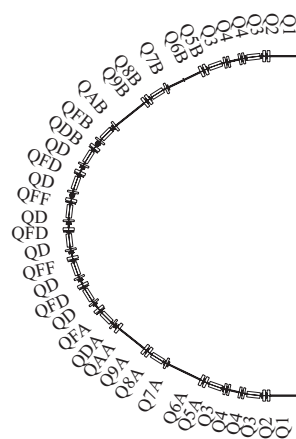The lattice configuration of the PF ring before the upgrade.

Figure 17
The new lattice configuration of the PF ring after the upgrade.

Table 4 List of the power supplies after the upgrade.

Q-mag family name	Power supply name	Type	Date of manu-facture	Maximum current [A]	Maximum voltage [V]	Capacity [kW]
Q1	PQ1	IGBT	2004	600	110	66
Q2	PNS	SCR	1997	600	130	78
Q3	PQ3	IGBT	2004	800	180	144
Q4	PQ4	IGBT	2004	800	180	144
Q5A	PQ5A	IGBT	2004	550	60	33
Q5B	PQ5B	IGBT	2004	550	60	33
Q6A	PQ6A	IGBT	2004	550	60	33
Q6B	PQ6B	IGBT	2004	550	60	33
Q7A	PQ7A	IGBT	2004	550	60	33
Q7B	PQ7B	IGBT	2004	550	60	33
Q8A	PQ8A	IGBT	2004	550	60	33
Q8B	PQ8B	IGBT	2004	550	60	33
Q9A	PQ9A	IGBT	2004	550	60	33
Q9B	PQ9B	IGBT	2004	550	60	33
Q10A	PIS	SCR	1997	450	50	22.5
Q10B	PJS	SCR	1997	450	50	22.5
QFD	PMS	SCR	1997	700	80	39.6
QFF	PDS	SCR	1997	900	150	39.6
QFA	PPS	IGBT	2000	700	50	35
QFB	PQS	IGBT	2000	700	50	35
QD	PHS	SCR	1997	750	190	142.5
QDA	PES	SCR	1997	900	45	40.5
QDB	POS	IGBT	2000	800	50	40
SFF	PKS	SCR	1997	450	140	63
SFD	PLS	SCR	1997	450	140	63
SD	PGS	SCR	1997	450	260	117

Figure 18
Photograph of the power supplies.

the electrical shunts were connected in parallel with the quadrupole magnet to divert a fraction of the magnetic current and reduce the field strength. For example, the quadrupole magnets of families Q9A and Q9B were connected to the power supply PMS, and a current bypass of about 82 A was made for the quadrupole magnets of family Q9 A by electrical shunt, as shown in Fig. 16. After the upgrade, the total number of the power supplies increased to twenty-three, the same as the number of the optical families. Thus, there is no longer any need for electrical shunts. The new configuration of the quadrupole magnets is shown in Fig. 17, and that of the power supplies in Table 4. For the new power supplies, the switching frequency of the IGBT (Insulated Gate Bipolar Transistor) device is 20kHz and the ripple of the output current is within $\pm 3.0 \times 10^{-5}$. A photograph of the new power supplies is shown in Fig. 18.

Reconstruction of beam ducts and upgrade of the vacuum control system

Due to the modification and rearrangement of the quadrupole magnets, the vacuum chambers in the upgraded straight sections, as well as their related bend sections need to be renewed. Based on the new vacuum system design, as reported in the 2002 and 2003 Photon Factory activity reports, the manufacture of all vacuum chambers including twelve bending chambers was completed by the end of FY2004. Vacuum leak checks for all of these chambers were carried out before installation to the ring. Thermal in-situ baking will be omitted because we expect that beam scrubbing effects due to synchrotron light irradiation will provide efficient cleaning. Pre-baking before installation was performed only for the chambers in the southern part of the ring. The purpose of this was to evaluate the effect of pre-baking in an early period of accelerator commissioning by comparing the vacuum pressures between the southern part and the northern part.

Prior to the major modification of the vacuum system in 2005, we upgraded the vacuum control system in the summer of 2004 [1]. The new vacuum control system is based on PLC (Programmable Logic Controller) and EPICS (Experimental Physics and Industrial Control System). The vacuum interlock system was also upgraded to a PLC-based system. With these upgrades, the reliability, operability and maintainability of the vacuum control system were improved.

Fig.19 shows the architecture of the PLC/EPICS-based vacuum control system. We installed new devices in the "User Interfaces", "I/O Controller", and "Device Interfaces (CPU/Relay)" layers. The Device Interfaces (CPU) are the PLCs, and for ethernet communication with the PLCs we adopted a software module developed by the KEKB control group,'EPICS Device/Driver Support for OMRON PLC'. Using this module EPICS can communicate with the PLCs using the original OMRON
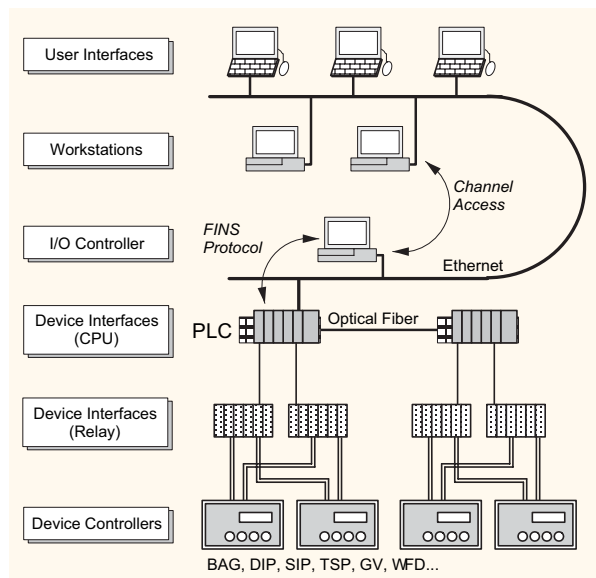

Figure 19
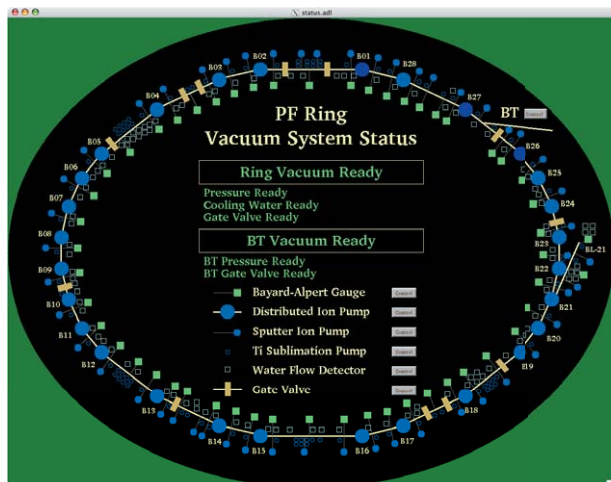Architecture of the PLC/EPICS-based vacuum control system.

Figure 20
Monitor panel of the vacuum system status.

Figure 21
Example spectra of the SGU radiation.

protocol (FINS protocol), so that EPICS can directly read or write I/O memories in the PLCs. For the "I/O Controller" we installed a software IOC running on PC/Linux instead of the widely used but expensive VME/IOC system. Also we installed relay modules for interfacing between the current device controllers and the new PLCs. Most of the vacuum device controllers (in the "Device Controllers" layer) remain unreplaced, and the workstations are shared with other groups.

Fig. 20 shows the monitor panel of the vacuum system status. Users can monitor and operate all of the vacuum devices (except rough pump systems) using similar control panels on network-connected PCs (in the "User Interfaces" layer).

References
[1] Y. Tanimoto, T. Nogami and T. Obina, *Proc. of PAC.*, (2005).

Construction of a very short period undulator (SGU#17) and the Photon Factory upgrade project

To increase the number of straight sections for insertion devices, an upgrade project of the PF ring is under way [1]. Due to the upgrade, four new 1.4-m straight sections will be created, and the existing ones will be nearly doubled in length. The 1.4-m straight sections are designed to have small betatron functions, so that in-vacuum type undulators with very short magnetic periods and gaps can be installed. Over the past few years, we have been developing short-period undulator magnets, and in 2004 we completed a short-period, short-gap in-vacuum undulator (SGU) at the 2.5 GeV Photon Factory storage ring as a practical source in the hard X-ray region for protein crystallography.

Even with the 2.5-GeV electron energy of the PF ring, it is possible to produce hard X-rays up to 15 keV by selecting a very short undulator period length, as shown by the spectra of Fig. 21. However, these spectra are only valid when the undulator can be set to a very short gap, of the order of 5 mm or less. This can be accomplished by a combination of in-vacuum undulator technology [2]
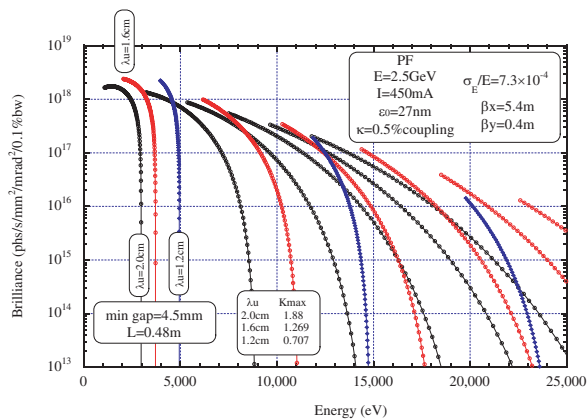
and an advanced lattice design with small betatron functions [3].

The completed in-vacuum undulator (SGU#17) is to be installed in the straight section between bending magnets B#16 and B#17 in the upgraded PF lattice. The vertical betatron function is designed to be 0.4 m at the center of this section, allowing a minimum gap of 4.5 mm for SGU#17. Below we describe the basic features of SGU#17.

The new undulator employs a pure Halbach-type magnet arrangement with a period length (λ_u) of 16 mm in order to obtain photon energies of up to 15 keV from the lower (1st to 7th) harmonics of the undulator radiation. Due to the available length at the installation site we have adopted a periodicity (N) of 29. For the magnet material we have selected an Nd-Fe-B alloy with a remanent field of Br=12.0 kG and a coercivity of iHc=28 kOe (NEOMAX35VH manufactured by NEOMAX Co. Ltd.), providing excellent magnetic performance and endurance against the high temperatures applied during baking. Magnet blocks made from this porous alloy are coated with a 5 μm layer of TiN for vacuum sealing, embedded in a holder made from oxygen-free copper, and attached to a pair of aluminium magnet-mounting beams. The magnet system components are enclosed in a stainless steel vacuum chamber with an electrolytically polished internal surface. The size of the chamber is 250 mm (inner diameter) × 980 mm, and it is evacuated using a combination of Ti sublimation pumps and sputter ion pumps. The magnet gap can be varied from 40 mm to 4.5 mm (with a deflection parameter K ranging up to 1.27), and is controlled by a translation system composed of precise ball screws and linear guides. The translation is transmitted to the magnet arrays using linear-motion feedthroughs and bellows coupling. In order to avoid problems due to Ohmic and parasitic mode losses, we cover the opposing faces of the magnet arrays with a thin metal foil made of oxygen-free copper (60 μm) plated with Ni (25 μm) for magnetic sustainment. The end of the magnet array is also connected to the Q-duct of the PF ring using a flexible 180 μm Be-Cu foil.

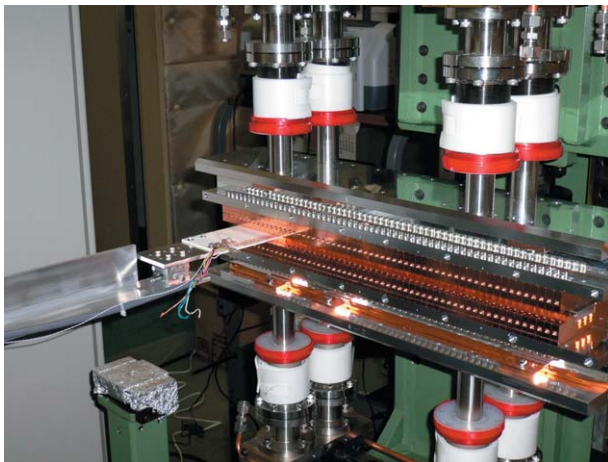Field adjustments have been made on the basis of precise field measurements using Hall probes ori-

Figure 22
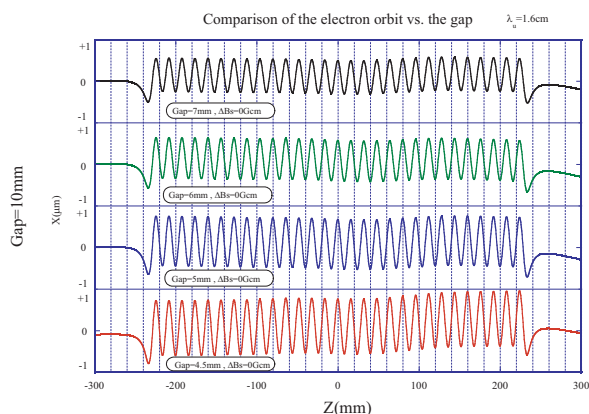Photograph of an SGU#17 during magnetic measurements.

Comparison of the electron orbit vs. the gap $\lambda_u=1.6cm$

Gap=7mm , ΔBs=0Gcm
Gap=6mm , ΔBs=0Gcm
Gap=5mm , ΔBs=0Gcm
Gap=4.5mm , ΔBs=0Gcm

Figure 23
Summary of the field measurements of the SGU in terms of the electron trajectory.

Figure 24
Calculated spectrum of the SGU with λu=16mm at K=1.05.

ented in the y- and x- directions, as shown in Fig. 22. We have adjusted the undulator field by optimizing the kick angle of the electron at each pole to produce an ideal sinusoidal orbit in the horizontal plane and also to have a straight orbit in the vertical plane. The adjustment method consists of (1) exchange of the magnet blocks and (2) insertion of disk-shaped magnet chips into holders in magnet blocks.

The results of the field adjustment are summarized in Fig. 23 in terms of the electron orbit in the undulator. The quality of the undulator fields is satisfactory within the allowed range of the gap, and field adjustment was carried out at a gap of 5 mm. We also have obtained satisfactory results for the kicks at the undulator entrance and exit that violate parallelism between the electron orbit and the undulator. We find that both the absolute values of the kicks and their relative changes are satisfactorily small. In Fig. 23 the kicks at the entrance are shown as a field integral, ΔBS (Gcm). The effects of the field errors on each harmonic can be described by the ratio of the real brilliance of the radiation to the ideal case. The real brilliance is calculated for the case of a single electron using the measured field data, whereas the ideal brilliance is calculated for the ideal field. In case of SGU#17, the brilliance ratio is as high as 94% for the fifth harmonic following
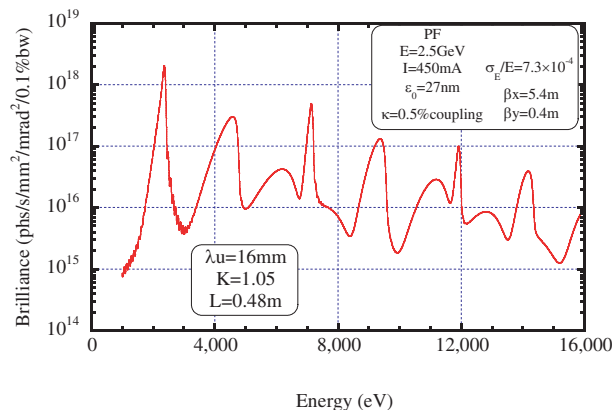
fine field adjustments.

Fig. 24 shows the radiation spectrum for SGU#17 at a gap of 5.4 mm (K=1.05). The calculation was made using the 2.5 GeV PF ring parameters given in the inset to the figure.

References

[1]   *Photon Factory Activity Report 2003,* **21A** (2004) 97.
[2]   S.Yamamoto, K. Tsuchiya and T. Shioya, *AIP Conf. Proc.,* **705**, (2004) 235.
[3]   *Photon Factory Activity Report 2002,* **20A** (2003) 82.

2-3 Research and Development

Top-up injection of the PF ring

The KEK linac is a 600-m long injector for four different storage rings (PF, PF-AR, KEKB e⁻ and e⁺). The KEKB rings are operated under continuous injection mode (CIM) with 10-Hz repetition in order to enhance integrated luminosity. The simultaneous injection of electron and positron beams is planned for the future Super-KEKB project. An upgrade of the linac to perform fast beam mode switching at up to 50 Hz so that each beam pulse can be injected into the PF ring, the PF-AR and the KEKB rings is planned by the injector upgrade committee (IUC). During the early discussions of the IUC, we have mainly focused on a fast beam switching system between the continuous-injection operation of of the KEKB and machine studies which need continuous injection at the PF or PF-AR. Since, by using this fast switching system, we can use the beam from the linac not only to carry out machine studies but also for the daily operation of the PF ring, we started to consider top-up injection for the PF ring. We plan to carry out the top-up injection of the PF ring in the following three phases.

Phase I. Construct an independent beam transport line in the third switching yard to extract the linac beam independently from the KEKB as shown in Fig. 25. Design common optics for the linac for both PF injection and KEKB injection. Install a pulsed bending magnet instead of a DC switching magnet in the entrance of the beam transport line. After these improvements, we can inject
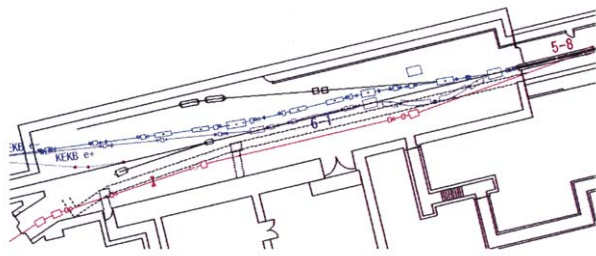
the beam into PF ring every 20 minutes.

Phase II. Establish pulse by pulse, and multi-energy fast switching system for the linac. After this improvement, we can operate the PF ring with top-up injection during the electron operation mode of the linac.

Phase III. Establish simultaneous acceleration of the electron and the positron beams of the linac. Afterwards, we can operate the PF ring with fulltime top-up injection.

In Phase I, a new PF-BT will be constructed in the third switching yard so that the BT line makes a detour to avoid the ECS magnets, as shown in Fig. 25. In autumn 2006, a pulsed bending magnet will be installed at the end of linac (5-8 unit) to allow fast beam switching to the PF ring. In Phases II and III, we will accelerate beams of different energy using the same lattice, with the lattice optimized for low-energy beam transmission. The phase of the low-level RF will be adjusted quickly to change the beam energy (multi-energy linac scheme). A feasibility study of this scheme has been already carried out, with the result that this method has no essential difficulties. The beam-orbit correction algorithm has been also designed and tested with a computer simulation, with positive results.

For Phase III, the fast beam mode switch will be added to the KEKB positron mode. For pulse by pulse switching between the electron and positron beams, we will use a special target assembly having a hole in the side. During two orbits of the electron beam, one will hit the target and other will pass through the hole, with pulse by pulse switching. The new target assembly will be installed in summer 2005, and tests of the fast electron and positron mode switching will start during the autumn run. For the injection of PF-AR, a fast beam mode switching system using the 3.5 GeV KEKB beam is currently being designed.

We have also started to perform top-up injection machine studies of the PF ring. Early results of these studies are described in the following articles.

A beam position monitor for undulators using the SR monitor technique

Monitoring the undulator radiation is an important problem for SR facilities. Since radiation from the neighbouring upstream and downstream bending magnet edges is superimposed onto the radiation from the undulator, it is difficult to monitor the undulator radiation inde-

pendently [1]. This problem is particularly serious for VUV undulators since the spectrum ranges of the undulator and the bending magnets are similar. To solve this problem, we apply the technique of optical SR monitoring.

The low-energy tail (visible light range) in the spectrum of the undulator radiation is emitted into a large opening angle, and can be seen surrounding the central sharp cone of the undulator radiation. This low-energy tail of the spectrum is extracted via water-cooled beryllium mirror which has a hole in the center to allow the main power of the undulator to pass through. In the same range of opening angle, both the bending radiation and the undulator radiation are emitted together. To separate these rays, we apply a focusing system similar to that used in the visible SR profile monitor. Since the conjugation distances from the source points for the bending magnets and the undulator are different, radiation from the different sources does not focus to the same point. Using this, we separate the undulator radiation from the bending magnet radiation.

The optical system of the monitor is installed in the BL-5 undulator beamline, as shown in Fig. 26. We insert a water-cooled Be-mirror with a central hole to extract the low-energy tail (visible light range) in the spectrum of the undulator radiation.

We applied an ordinal focusing system similar to that used in optical profile monitors to produce an image of the beam in the undulator [2]. The central hole of the Be-mirror is not only used to pass the powerful radiation cone, but also has an important optical function. When we focus the light from the undulator source point, the defocused light from the bending magnets is simultaneously overlapped in the same focus plane. When the mirror has a hole in the centre, the defocused bending magnet light becomes a ring pattern surrounding the image of the undulator light, as shown in Fig. 27. We can select just the undulator light by masking this defocused ring pattern. After this processing, we can observe the undulator light only. The beam image from the undulator is shown in Fig. 28, and the image from the downstream bending magnet in Fig. 29. The values of the β
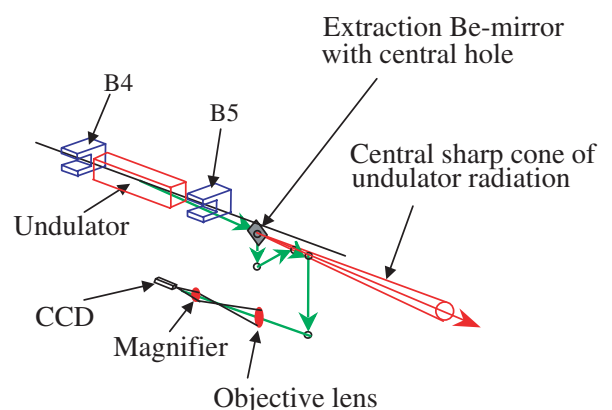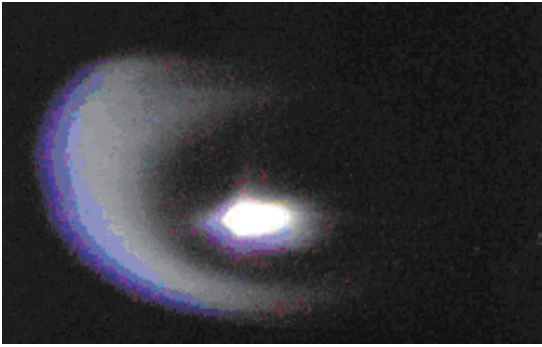
Figure 27
Image of the undulator light (central bright spot) with defocused light from the downstream bending magnet.
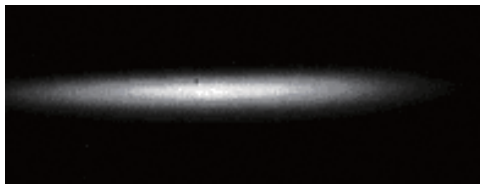

Figure 28
Separated beam image from the BL-5 undulator. The undulator gap is 140 mm (K=0.56).
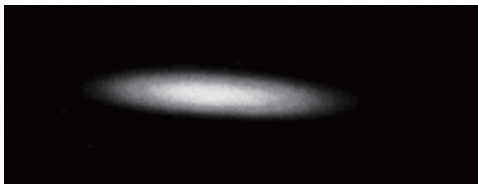

Figure 29
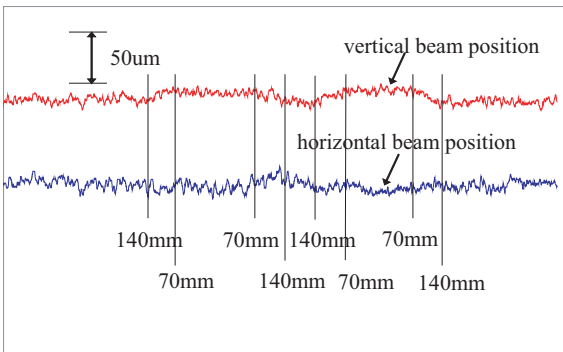Separated beam image from the BL-5 bending magnet.

Figure 30
Results of beam position measurements while changing the undulator gap from 140 mm to 70 mm.

-function for the undulator source point are β_x=10.25 m and β_y=8.64 m, and those for the bending magnet source point are β_x=2.69 m and β_y=8.48 m, so the undulator beam profile has a large horizontal beam size compared to the beam from the bending magnet.

We use a simple position analysis with a centroid calculation to obtain the vertical and the horizontal beam positions. We observed the vertical and the horizontal beam position in the undulator while changing the gap from 140 mm to 70 mm, corresponding to K values of 0.56 and 4.13. Results of these beam position measurements are shown in Fig. 30. When the gap of undulator

changes from 140 mm to 70 mm, the vertical beam position moves by about 10 μm. No systematic movement in the horizontal direction was observed. The vertical and the horizontal beam positions were measured once per second.

References
[1] G. Decker, O. Singh H. Friedsam, J. Jones, M. Ramanathan and D. Shu, *Proc of PAC'99,* (1999) 2051.
[2] T. Mitsuhashi and M. Katoh, *Proc of EPAC'96,* (1996) 1669.

Observation of a coherent oscillation of the stored beam due to the non-linear kick of the sextupole magnet

A coherent oscillation of the stored beam is often excited by an error in the injection pulse bump. A non-linear kick by the sextupole magnet which is set inside the injection pulse bump also excites a coherent oscillation of the stored beam. Since these oscillations are excited during every injection, they present a serious problem when considering top-up operation of the storage ring. If there are no non-linear magnets such as the sextupole magnet in the injection pulse bump, the coherent oscillation of the stored beam can be reduced by correcting the pulse bump error. But due to the non-linear kick of the sextupole magnet, an extra oscillation of the stored beam will be excited during the rising and falling in the pulse bump. We have investigated the coherent oscillation due to the non-linear kick of the sextupole magnet using an SR monitor system incorporating a fast-gated camera [1]. The source point of this monitor is in the bending magnet 27, it is the second bending magnet in the injection bump. The coherent oscillations during the 16 turns following the excitation are recorded in one frame of the camera, and we have observed the oscillation with the excitation positioned at 200 ns intervals during the injection pulse, as shown in Fig. 31.

The observed beam oscillations with the sextupole magnet switch ON (left) and OFF (right) are shown in Fig. 32.

As shown in the left-hand column of Fig. 32, the oscillation of the beam is only suppressed at excitation
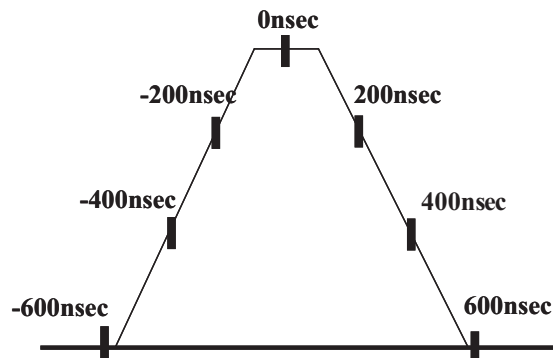

Figure 31
The relation between measuring points and the pulse shape of the injection bump.

-600 nsec

-400 nsec

-200 nsec

0 nsec (center)
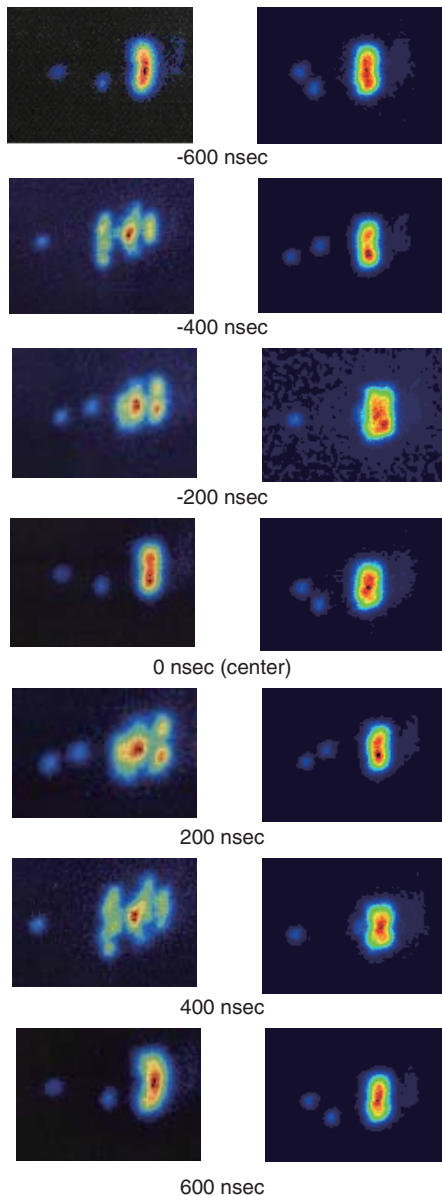
200 nsec

400 nsec

600 nsec

Figure 32
The observed beam oscillation with the sextupole magnet switch ON (left column) and OFF (right column). Sixteen turns of beam oscillations are superimposed on each frame. One or two beam spots on the left side of the images corresponds the beam which comes just at the timing of the injection pulse bump is exited.
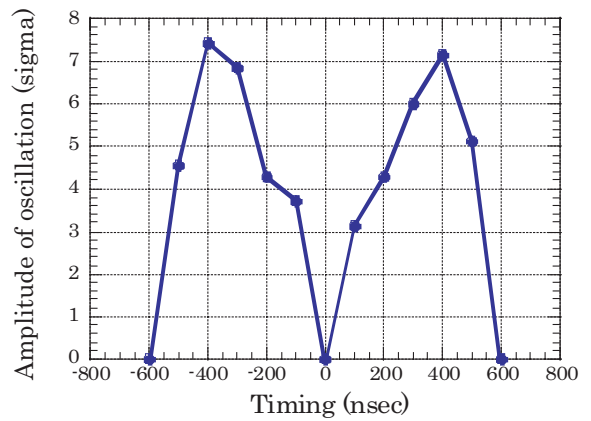

Figure 33
Amplitude of the coherent oscillation of the stored beam with the sextupole magnet switch ON as a function of excitation timing.
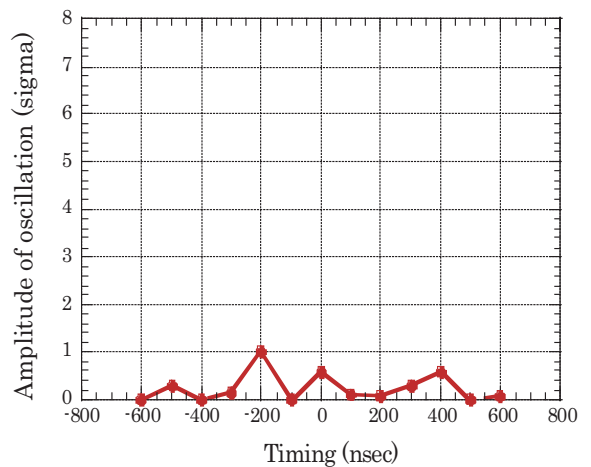

Figure 34
Amplitude of the coherent oscillation of the stored beam with the sextupole magnet switch OFF as a function of excitation timing.

timings of ±600 nsec and 0 nsec. At other timings during the rise and fall of the injection pulse bump, we observed large oscillations excited by the non-linear kick of the sextupole magnet. The oscillation of the stored beam seems to show similar patterns at symmetrical timings (at ±400 nsec, and ±200 nsec) relative to the centre of the pulse. Although the intensity of the pulse bump is only 25% of the peak intensity at ±400 nsec, large oscillations of the stored beam were observed. The amplitude of the coherent oscillations with the sextupole magnet switched on as a function of excitation timing is shown in Fig. 33. Observations of the oscillations of the stored beam with the sextupole magnet switch OFF are shown in the right-hand column of Fig. 32. The oscillations are almost suppressed for all excitation timings. The amplitude of the coherent oscillation with the sextupole magnet switched off as a function of excitation timing is shown in Fig. 34.

The maximum amplitude of the oscillation is about 1σ of the horizontal beam size. The remaining oscillation of the beam is excited by the errors in the four kicker magnets.

In all observations, we observed vertical oscillation of the stored beam, even where horizontal oscillation is suppressed. We consider that this vertical oscillation is due to rotation errors in the alignment of the quadrupole magnet.

References
[1] A. Ueda, T. Mitsuhashi, K. Harada and Y. Kobayashi, *Proc. of EPAC'04*, (2004) 71.

Observation of quadrupolar-wakefield effects by means of quadrupolar-tune measurements

Modern synchrotron light sources have many vacuum chambers with no axial symmetry, for example flat chambers for short gap undulators. When the stored electron beam passes through these non-symmetric structures, the motion of the beam is affected not only by the mono-polar and dipolar components of the induced wakefields, but also by quadrupolar and higher-order components. Effects due to the quadrupolar component of the resistive

wakefield has been observed [1] in the PEP-II B-factory and other storage rings. Effects due to short-range quadrupolar wakes were also observed for proton beams in the Super Proton Synchrotron (SPS) at CERN [2]. To improve understanding of the beam dynamics, it is very important to measure the contributions from the dipolar and quadrupolar wakes separately. We have showed in the Photon Factory that this can be done by measuring both the coherent tunes of the dipolar and quadrupolar betatron oscillations [3].

The coherent tunes of the dipolar (beam-centroid) oscillations can be measured using a conventional RF knockout method. The other quadrupolar (bunch shape) oscillations can be excited [4] by applying ac quadrupole fields oscillating at a frequency of $2f_r \cdot \Delta\nu$, where f_r is the revolution frequency and $\Delta\nu$ is the fractional betatron tune. Figs. 35(a) and (b) show the measured quadrupolar tunes [3] as a function of the bunch current under single bunch operation. These figures show remarkable shifts in the quadrupolar tunes. The signs of the tune shifts were found to be opposite for the horizontal and vertical oscillations. This result can be explained by a self-focusing effect due to the quadrupolar component of the short-range wakefields. The induced wakefields focus the bunch in the horizontal direction, and defocus it in the vertical direction.
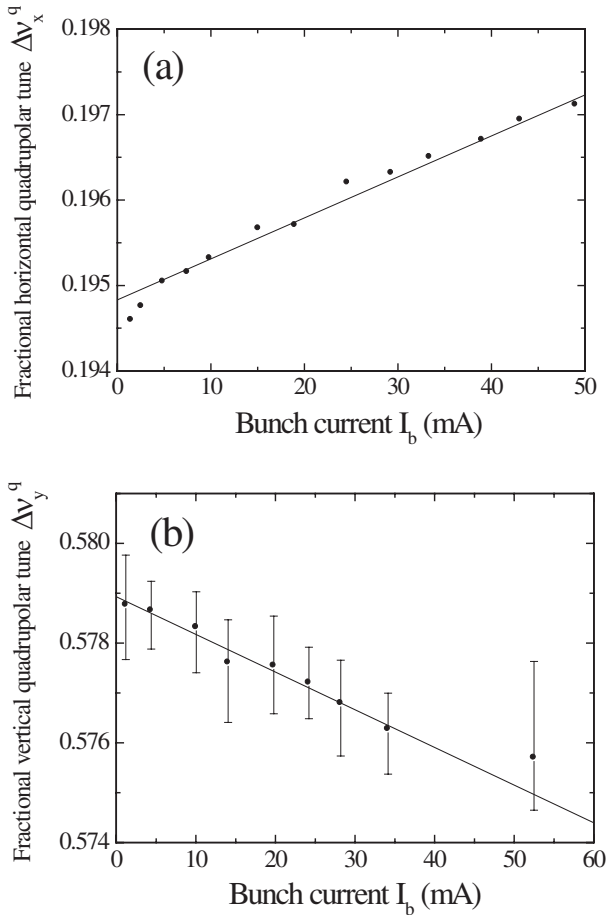
Table 5
Summary of the measured tune shifts under single bunch operation.

	Horizontal	Vertical
Dipolar tune shift	-0.013 A^{-1}	-0.11 A^{-1}
Quadrupolar tune shift	0.048 A^{-1}	-0.076 A^{-1}

Table 6
Estimated dipolar and quadrupolar kick factors. Average betatron functions ($\beta_x \sim 3.1$ m, $\beta_y \sim 6.9$ m) were used.

	Horizontal	Vertical
Dipolar kick factor $k^{(1)}$	610 Vm^{-1}pC^{-1}	520 Vm^{-1}pC^{-1}
Quadrupolar kick factor $k^{(2)}$	-390 Vm^{-1}pC^{-1}	280 Vm^{-1}pC^{-1}

rection. A summary of the measured tune shifts is given in Table 5.

The dipolar ($\delta\nu_x^{\mathrm{d}}$) and the quadrupolar ($\delta\nu_x^{\mathrm{q}}$) tune shifts in the horizontal direction are approximately given by,

$$\delta\nu_x^{\mathrm{d}} = -\frac{q_b e}{4\pi E} \sum_j \beta_x(s_j) \left[k_{x,j}^{(1)} + k_{x,j}^{(2)} \right], \quad (1)$$

and

$$\delta\nu_x^{\mathrm{q}} = -\frac{q_b e}{2\pi E} \sum_j \beta_x(s_j) \cdot k_{x,j}^{(2)}, \quad (2)$$

where q_b is the bunch charge, E is the beam energy, e is the electron charge, $\beta_x(s_j)$ is the betatron function at position s_j, and $k_{x,j}^{(1)}$ and $k_{x,j}^{(2)}$ denote the kick factors of the j-th component due to the dipolar and quadrupolar wakefields. Using these relations, we can estimate both the dipolar and quadrupolar kick factors, as given in Table 6. This method of diagnosing the transverse wakefields can improve our understanding of the beam dynamics in electron storage rings.

References
[1] A. Chao, S. Heifets and B. Zotter, *Phys. Rev. ST Accel. Beams,* **5** (2002) 111001.
[2] J. Gareyte, *Proc of the Eighth European Particle Accelerator Conference,* (2002) 89; H. Burkhardt, G. Rumolo and F. Zimmermann, ibid., 1449
[3] S. Sakanaka, T. Mitsuhashi and T. Obina, *Phys. Rev. ST Accel. Beams,* **8** (2005) 042801.
[4] S. Sakanaka, Y. Kobayashi, T. Mitsuhashi and T. Obina, *Jpn. J. Appl. Phys.,* **42** (2003) 1757.

Beam test of transverse bunch-by-bunch feedback system

Transverse bunch-by-bunch feedback controls the betatron motion of each bunch independently and is widely used to cure transverse beam instabilities. The beam test of a transverse bunch-by-bunch feedback system using FPGA (Fileld Programmable Gate Array) as a digital signal processor was performed at the PF ring with 500 MHz bunch rate. A damping time of 1 ms was obtained both in the horizontal and the vertical planes,
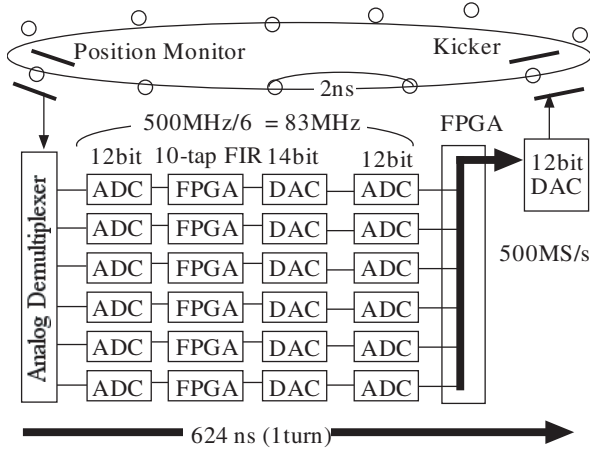
Figure 36
Block diagram of the bunch-by-bunch feedback system used in the test. This system is a prototype, and includes an unnecessary analog data passing stage (DAC-ADC) which will be eliminated in the new system planed for the Photon Factory ring.

a value one order of magnitude smaller than that of the radiation damping. The feedback system was used to successfully suppress the vertical coupled-bunch instability observed during usual operation. It was also quite effective for damping the coherent beam oscillations during beam injection. This feedback system will take the place of the octupole magnets for suppressing the vertical instability. As the octupole fields cause a reduction of dynamic aperture for the injection beam, the transverse feedback system will be indispensable for the future top-up operation of the PF ring.

A block diagram of the feedback system is shown in Fig. 36. The system is the first in the world which can handle betatron motions in both the horizontal and vertical planes with just one feedback loop, which is realized with a newly developed signal-processing scheme and the processing power of FPGA. 12-bit ADCs are employed in order to obtain simultaneously both high resolution and wide dynamic range. The system was developed at SPring-8.

Growth and suppression times of an ion-related vertical instability

In the PF-ring, a vertical instability is observed in the multi-bunch operation mode. Since this instability depends on the vacuum conditions in the ring, it is assumed that it is caused by the ion trapping effect. The instability can be suppressed by Landau damping with octupole magnetic fields [1]. Since the operating parameters during routine operation are close to the instability threshold, the octupole magnets are excited during user operation.

In the PF ring, there are four DC octupole magnets which are operated at the same time. In multi-bunch operation mode the PF ring is operated with 280 bunches, and the remaining 32 empty buckets are used for ion-cleaning. Under these conditions, the DC octupole field strength at the threshold of the instability, $K_{3,th} = (L/B_0\rho) \partial^3 B_x / \partial y^3$, is about 158 m^{-3}, and the instability is suppressed when the DC octupole field strength is larger

than $K_{3,th}$. On the other hand, the instability grows when the field strength is smaller than $K_{3,th}$. Here B_x is the horizontal component of the magnetic field, L is the effective length of the octupole magnet and $B_0\rho$ is the magnetic rigidity of the electron.

In order to study the dynamical behavior of the instability, we use a pulsed octupole magnet system [2]. Using this system, we can measure the growth and suppression times of the instability by using a real-time spectrum analyzer (Tektronix, RSA230) to observe the response of the beam spectrum from a button-type electrode when the octupole field rises or falls [3]. Fig. 37 shows the beam spectra in the vicinity of the second harmonic of the RF frequency f_{rf} when the instability is a) excited and b) suppressed. When the instability is excited, 6 peaks of the betatron sideband are observed, for example at $2f_{rf} - f_{rev} - f_{\beta y}$, where f_{rev} is the frequency of the revolution and $f_{\beta y}$ is the vertical betatron frequency.

We performed the experiments under two different conditions: a constant bunch number of 280 bunches and a constant bunch current of 1.6 mA. With these conditions we can investigate the effects of fill pattern and bunch current. It seems that these effects relate to the phenomena of ionization and ion trapping.

For measurement of the instability growth time, we adjusted the DC octupole magnets to $K_{3,dc} = 208$ m^{-3}, providing stable initial conditions with no beam instability. The instability was only observed when the pulsed octupole magnet was excited. Thus, we excited the pulsed octupole magnet from zero to $K_{3,p} = -315$ m^{-3} in 1.2 ms. Fig. 38 shows the response of the power spectrum at $2f_{rf} - f_{rev} + f_{\beta y}$ to the excitation current of the pulsed octupole magnet during the growth process of the instability. The instability appeared 12 ms after the excitation of the pulsed octupole field, showing an exponential growth. We can thus conclude a time of 12 ms for the delay time
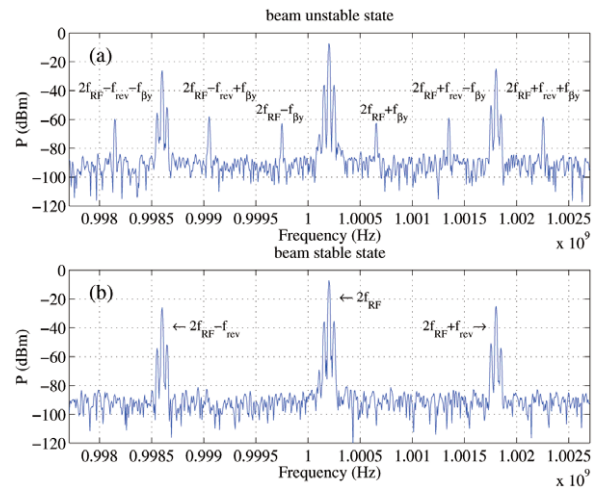

Figure 37
Beam spectrum from a button-type electrode when the pulse octupole magnet was excited at $K_{3,p} = 315$ m^{-3}. The beam current was 432 mA with 280 bunches. (a) The spectrum of the beam unstable state when the vertical instability was excited. (b) The spectrum of the beam stable state when the instability was suppressed.
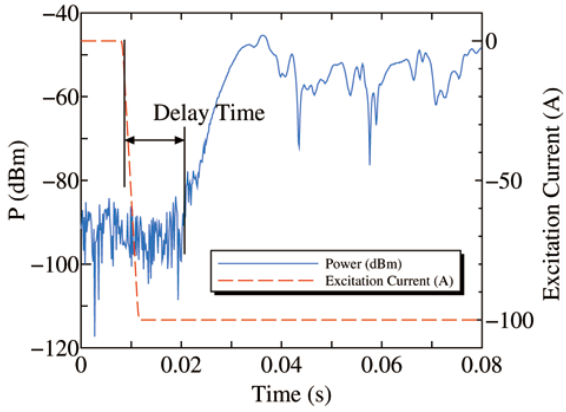
Figure 38
The response of the power spectrum at $2f_{rf} - f_{rev} + f_{\beta y}$ (solid line) to the excitation current of the pulse octupole magnet (dashed line) during the growth process of the instability. The pulse octupole excitation current of -100 A corresponds to $K_{3,p} = -315$ m^{-3}, and the beam current was 432 mA with 280 bunches.
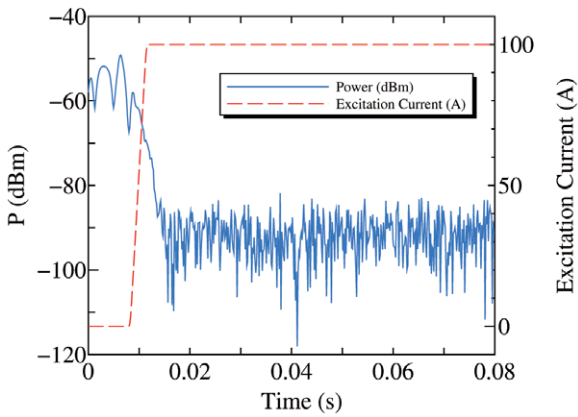

Figure 39
The response of the power spectrum at $2f_{rf} - f_{rev} + f_{\beta y}$ (solid line) to the excitation current of the pulse octupole magnet (dashed line) during the suppression process of the instability. The pulse octupole excitation current of 100 A corresponds to $K_{3,p} = 315$ m^{-3}, and the beam current was 432 mA with 280 bunches.

Figure 40
The delay times and the instability growth and suppression rates for a constant bunch number of 280. (a) The delay times for growth and suppression of the instability. (b) The instability growth and suppression rate.

of the instability growth process. In addition, we can define the growth rate of the instability as the slope of the power spectrum, calculated here to be 4 dBm/msec.

For measurement of the suppression time, we adjusted the DC octupole magnets to $K_{3,dc} = 131$ m^{-3}. Under the initial conditions, the instability peak always appeared. However, when we excited the pulsed octupole magnet from zero to $K_{3,p} = 315$ m^{-3}, the peak rapidly disappeared. Fig. 39 shows the response of the power spectrum at $2f_{rf} - f_{rev} + f_{\beta y}$ to the excitation current of the pulsed octupole magnet during the suppression process. We found that the instability suppression was almost simultaneous with the excitation of the octupole field.

Fig. 40 shows the delay times and the growth and suppression rates of the instability for a constant bunch number of 280. The error bars shown in the figure include only the statistical errors. For the measurements, three beam currents were selected; 100, 200 and 432 mA, and the delay times and rates calculated from the spectrum of $2f_{rf} - f_{rev} + f_{\beta y}$. During the growth process of the instability, the delay time increases as the beam current decreases. On the other hand, the delay time is al-
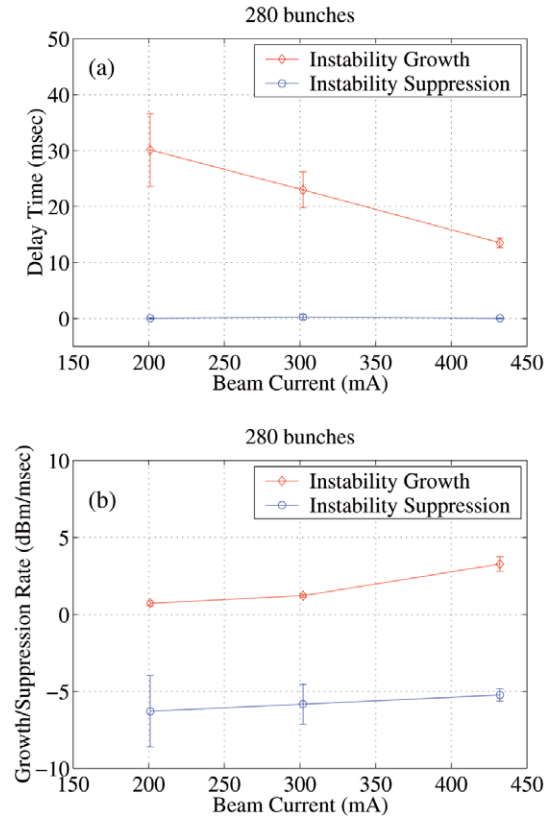
most zero and doesn't depend on the beam current in the suppression process. The absolute value of the growth rate is smaller than the absolute value of the suppression rate. In other words, the suppression process is slower than the growth process.

Fig. 41 shows the delay times and the growth and suppression rates for a constant bunch current of 1.6 mA and bunch numbers of 100, 200 and 280. In the growth process, the delay time increases as the bunch number decreases whereas the delay time is almost zero for the suppression process. This is the same as the result for a constant bunch number of 280.

For the growth process of the instability, longer delay times were observed in comparison to the suppression process. The delay time depends on the bunch current and the fill pattern of the bunch train, namely, the gap between the bunches available for ion-cleaning. Therefore, it seems that the process of ionization and ion-trapping is slow, and the time scale of the process is several tens of ms. On the other hand, in the suppression process of the instability, the delay time was less than a few hundreds of µs. We propose that the suppression is due to decoherence of the coherent motion of the beam due to the tune spread which is produced by the octupole field. Since this is a much faster process, it was simultaneously observed with the excitation of the octupole field.
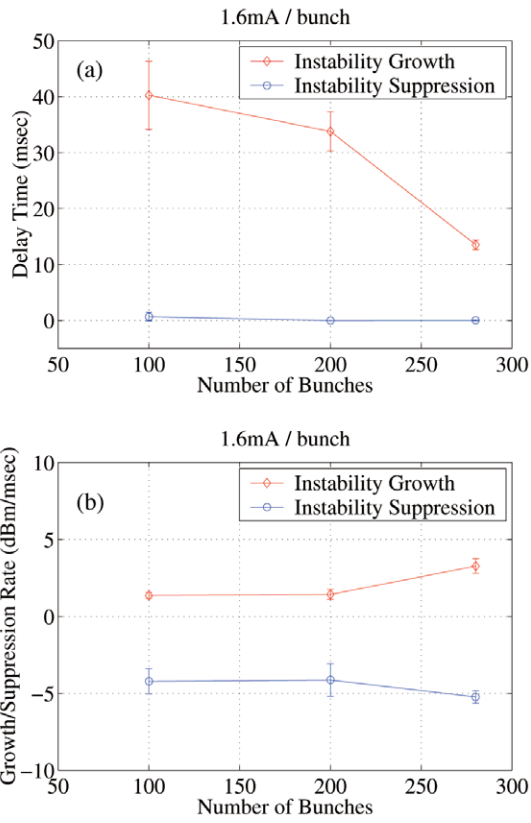
Figure 41
The delay times and the instability growth and suppression rates for a constant bunch current of 1.6 mA. (a) The delay times for growth and suppression of the instability (b) The instability growth and suppression rate.

References

[1] Y. Kobayashi and K. Ohmi, *Proc. Sixth European Particle Accelerator Conf.*, (1998)1288.

[2] T. Miyajima, Y. Kobayashi and S. Nagahashi, *Proc. of 2003 Particle Accelerator Conf.*, (2003) 2171.

[3] T. Miyajima, Y. Kobayashi and S. Nagahashi, *Proc. Ninth European Particle Accelerator Conf.*, (2004) 2095.